Ocean Modelling 168 (2021) 101896

Contents lists available at ScienceDirect

Ocean Modelling

journal homepage: www.elsevier.com/locate/ocemod

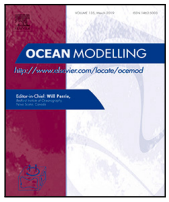

Vertical coordinate and resolution dependence of the second moment turbulent closure models and their limitations

Yalin Fan *, Zhitao Yu, Gregg Jacobs

Naval Research Laboratory, Stennis Space Center, MS, USA

ARTICLE INFO

Keywords:
Second moment turbulent closure models
Vertical coordinate
Vertical Resolution
Mixed layer enhanced grid
Near inertial gravity waves

ABSTRACT

Coordinate and resolution dependence of three second moment turbulent closure models are studied using one-dimensional Navy Coastal Ocean Model (NCOM) experiments and large eddy simulations at Ocean Station Papa. Our results suggest that finer resolution near the base of the mixed layer is critical for better model performance. A mixed layer enhanced vertical grid is proposed that outperforms both the uniform and the stretched grids with significantly fewer vertical layers used. For the new grid, the model accuracy is strongly dependent on the resolution near the base of the mixed layer, and not affected much by the total number of vertical layers used. However, given the success of the new grid, the lack of representation for the near inertial gravity waves below the mixed layer has hampered the ability of second moment turbulent closure models on accurate representation of turbulent mixing in the water column. While both the Langmuir circulation and the variation of surface heat fluxes are shown to be able to significantly change the strength of the near inertial waves, they have negligible effect on the eddy viscosity in the transition layer.

1. Introduction

Turbulent mixing plays an important role in the transport of momentum, heat, and particles across the mixed layer, and is critical to the vertical distribution of heat and salinity in the water column. Although the structure of turbulent eddies can be simulated by direct numerical simulations or large-eddy simulations, it is too expensive and unrealistic to solve for the turbulence in geophysical models for timely predictions of the flow fields over large areas such as those of Metzger et al. (2017) and Rowley and Mask (2014). Thus, parameterizations are required to provide an idealized description of turbulence with a reasonable compromise between cost and accuracy. Second moment turbulent closure (SMTC) models are among the most popular approaches used to parameterize turbulence in the geophysical models.

The Mellor–Yamada level 2.5 model (Mellor and Yamada 1982, hereafter MY2.5) has been used in many ocean and atmosphere models during the past several decades. Although there are some major shortcomings of the method that lead to smaller critical Richardson number and shallower boundary layer depth (Canuto et al., 2001; Cheng et al., 2002), it is still popularly used because the scheme considers the energetics of the mixing explicitly by solving diagnostic and prognostic equations, respectively, for the turbulent kinetic energy (TKE) and turbulent length scale. Since these equations carry information about the time history of the turbulence and thus can account for both advection and diffusion of the TKE. As people gradually recognized the importance of surface gravity waves in upper ocean mixing through Langmuir turbulence, Kantha and Clayson (2004, hereafter KC04) added vortex forcing to the Mellor–Yamada type SMTC model to represent the effect of surface waves, and their scheme has been adapted into several ocean circulation models. Later on, Harcourt (2015, hereafter H15) further improved the SMTC model by incorporating the vortex forcing in the stability equations as well. These three SMTC models are currently implemented in the Navy Coastal Ocean Model (NCOM). Note, Kantha et al. (2010) has pointed out that the value of closure constant E_6 was reported incorrectly in KC04 and recharacterized it to be 7.2 instead of 4.0. This correction has been adapted into NCOM, although the model is still labeled KC04.

Aside from turbulent mixing schemes, the choice of vertical coordinate system is another important aspect of the ocean model's design. As pointed out by Griffies et al. (2000), the representation and parameterization of processes not resolved by the model grid are often directly linked to the vertical coordinate choice. While many ocean models have flexible choices for vertical coordinate systems and resolution, it is unclear how these choices influence the representation of the boundary layer eddy effects under various turbulent closure models. In this study, we will address the coordinate and resolution dependence of the MY2.5, KC04, and H15 schemes and explore their limitations in turbulence representations using NCOM and large eddy simulation experiments. The data and methods are described in Section 2, results are analyzed in Section 3, and discussion and concluding remarks are presented in Section 4.

* Correspondence to: Oceanography Division, Naval Research Laboratory, Stennis Space Center, MS 39529, USA.
E-mail address: yalin.fan@nrlssc.navy.mil (Y. Fan).

https://doi.org/10.1016/j.ocemod.2021.101896
Received 12 December 2020; Received in revised form 9 September 2021; Accepted 7 October 2021
Available online 19 October 2021
1463-5003/Published by Elsevier Ltd.

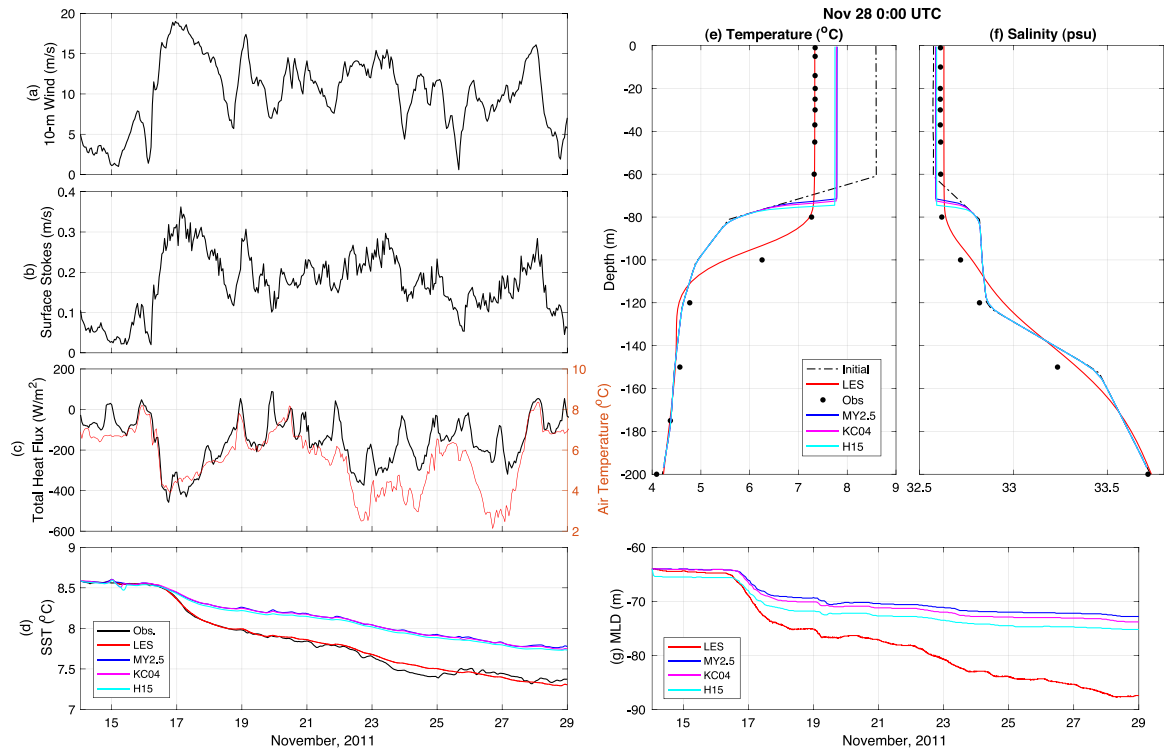

Fig. 1. (a) 10-m wind speed (m/s), (b) surface Stokes drift velocity (m/s), (c) total heat flux (W/m^2) and air temperature (°C) observed at the Ocean Station Papa from November 14 1 UTC to November 29 0 UTC. (d) Sea surface temperature (SST) (°C) comparisons among observations (black), LES results (red), and MLEG100 results using the MY2.5 (blue), KC04 (magenta), and H15 (cyan) scheme from November 14 1 UTC to November 29 0 UTC. (e) Temperature and (f) salinity vertical profile comparisons among the observations (black dot), LES results (red), and MLEG100 results using the MY2.5 (blue), KC04 (magenta), and H15 (cyan) scheme on November 28 at 0 UTC. (g) Mixed layer depth (MLD) comparisons among the LES results (red), and MLEG100 results using the MY2.5 (blue), KC04 (magenta), and H15 (cyan) scheme from November 14 1 UTC to November 29 0 UTC.

2. Method

2.1. Observational data

Hourly meteorological (10-m wind, net surface heat flux) and oceanographic (temperature, salinity) data for this study are obtained from the moorings at Ocean Station Papa (OSP) operated by the Ocean Climate Stations (OCS) group at Pacific Marine Environmental Laboratory of the National Oceanic and Atmospheric Administration (NOAA/PMEL) (Send et al., 2010). OSP is a deep-water station (with a water depth of more than 4 km) located at (144.9°W, 50.1°N), ~850 miles off the British Columbia coast. The station is within the subpolar northeastern Pacific gyre, and thus experiences strong and frequent winter storms. For this study, a 15-day period starting from 14 November 2011 at 1UTC was selected when OSP experienced large variations in wind forcing and several cooling events. The wind speed was low and mostly below 5 m s^{-1} during the first two days, and then rapidly strengthened to more than 20 m s^{-1} by the end of November 16 (Fig. 1a). At the same time, large sensible and latent heat fluxes at the ocean surface associated with the powerful winds led to a strong net cooling flux (~450 W m^{-2}) that closely follows the variation of the air temperature (Fig. 1c). The variation of the sea surface temperature (SST), on the other hand, is gradual and at much lower frequency (Fig. 1d). The winds gradually weakened while fluctuating afterwards with several weak cooling events associated with short periods of wind speed increases.

Concurrent detailed two-dimensional wave spectra, $E(\sigma,\theta)$, were collected nearby by the Applied Physics Laboratory at the University of Washington using a 0.9 m Datawell directional waverider (Thomson et al., 2013). Here σ and θ are the frequency and direction of the spectra. Hourly Stokes drift profile time series were computed from $E(\sigma,\theta)$ following Kenyon (1969):

$$\vec{u}_s(z) = 2\iint \sigma\vec{k}E(\sigma,\theta)e^{-2kz}d\sigma d\theta \quad (1)$$

where $\vec{k}$ is the wave number vector of the spectra. The variation of the surface Stokes drift closely follows the variation of the wind speed during most of the 15-day period (Fig. 1b), indicating wind sea dominance at the location.

2.2. The Navy Coastal Ocean Model (NCOM) experiments

NCOM is a hydrostatic model that solves the primitive equations. It uses a staggered Arakawa C grid with elevation and the main scalar (temperature and salinity) fields defined at the grid-cell centers and velocities defined at the center of the grid-cell faces. Turbulence fields for the mixing models and the vertical eddy coefficients are defined at the center of the top face of the grid cells where the vertical velocity points are defined. Aside from the two vertical grid types (uniform and uniformly-stretched) implemented, the model can also use vertical grids specified by the user through external input files. More details on the model can be found in Martin (2000). In this study, we use one-dimensional NCOM to test the performance of the MY2.5, KC04, and H15 schemes at OSP.

We only simulate the top 200 m of the water column because the observations suggest that the mixed layer depth (MLD) varied between 60 and 88 m during our simulation period. For each turbulent closure model, experiments are conducted for three types of vertical grids with 5 grid resolution options (30, 40, 50, 80, and 100 layers).

The uniform grid (UG), as the name suggests, uses constant spacing between model vertical grid points throughout the water column (Fig. 2a dotted lines). The uniformly-stretched grid (USG), also known as logarithmically-stretched grid, is designed so that each layer is thicker than the layer above by a fixed percentage. Thus, the grid

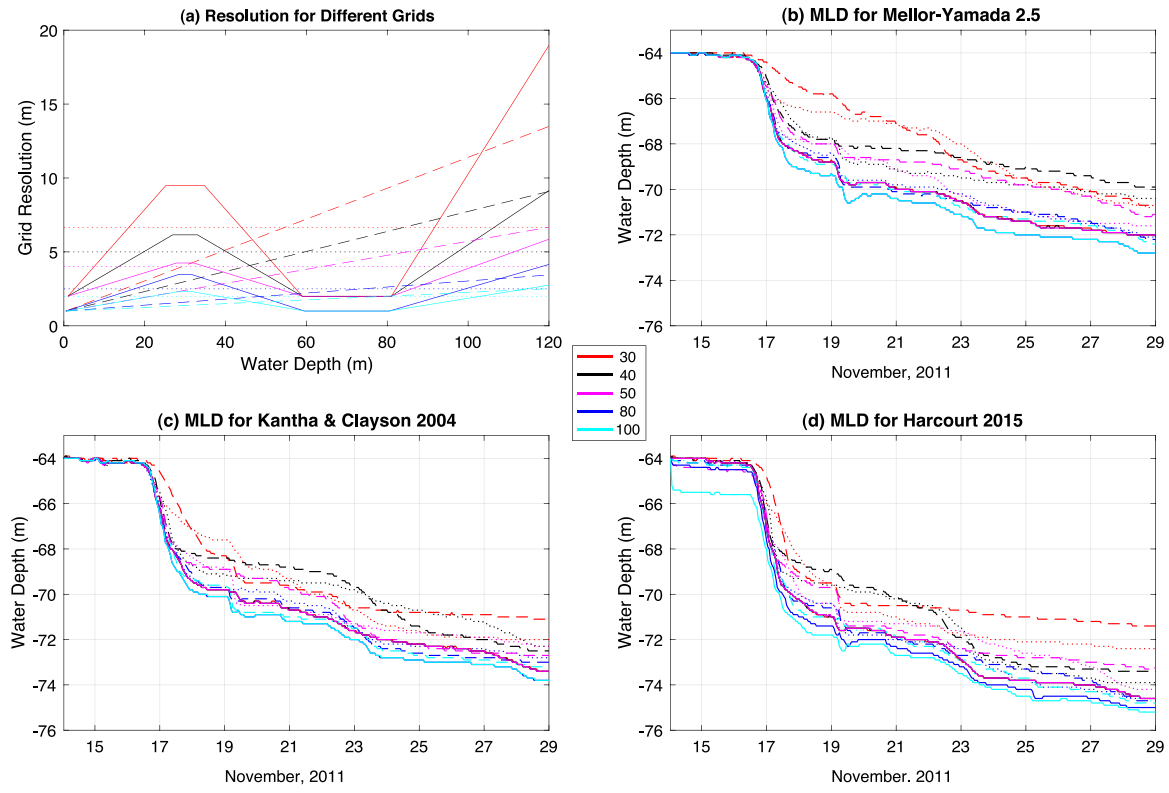

Fig. 2. (a) Vertical resolution corresponding to water depth for the UG, USG, and MLEG grids. Mixed layer depth (MLD) using the (b) Mellor–Yamada 2.5 (MY2.5), (c) Kantha & Clayson 2004 (KC04), and (d) Harcourt 2015 (H15) schemes. In all four panels, dotted, dashed, and solid lines represent the UG, USG, and MLEG grid type respectively. The color of the lines represents the number vertical layers used as given in the legend.

achieves higher resolution near the water surface (Fig. 2a dashed lines). All five USG grids use 1 m resolution at the surface. The stretch factor for each grid is determined based on the number of layers chosen within the 200 m vertical model domain for that particular grid, which are 11.03%, 7.01%, 4.86%, 2.06%, and 1.28% for the 30-, 40-, 50-, 80-, and 100-layer grid respectively.

This study also proposes a third type of vertical coordinate system, the mixed layer enhanced grid (MLEG), which uses higher resolution both at the water surface and near bottom of the mixed layer (Fig. 2a solid lines). The detailed design of the MLEG is illustrated in Fig. 3. The vertical model domain is separated into three regions: region 1 goes from the surface to the top of the mixed layer base (at 60 m depth in this study); region 2 goes from top to bottom of the mixed layer base (between 60 and 80 m in this study); and the water column below the bottom of the mixed layer base is region 3.

In region 1, the grid is first uniformly stretched from surface to the midpoint of the region. The resolution in the first layer is set to be the minimum resolution of Δz_{min}(2 m for the 30-, 40-, and 50-layer cases and 1 m for the 80- and 100-layer cases in this study). Then the vertical grid is reversely uniform stretched from the midpoint to the bottom of region 1 (top of the mixed layer base) where the resolution is reduced back to Δz_{min}. Thus, in region 1, the grid points above and below the midpoint are symmetrically distributed about the midpoint. In region 2, uniform grid is used with resolution Δz_{min}. In region 3, the grid is uniformly stretched from the bottom of the mixed layer base to the bottom of the model domain.

The results of the NCOM simulations are presented in Section 3 where all experiments are represented by the grid type and layer numbers. For example, experiment UG50 represents uniform grid with 50 layers.

2.3. The Large eddy Simulation (LES) model

The NCAR LES solves the wave-phase-averaged Craik–Leibovich equations (Craik and Leibovich, 1976) to include the effect of surface gravity waves through vortex force, Stokes–Coriolis force, Lagrangian mean advection associated with Stokes drift, and a wave averaged increment to pressure that arises through conservative wave–current interactions. Detailed model formulations have been reported in existing publications (e.g. McWilliams et al., 1997; Sullivan et al., 2007) and are not repeated here. LES models differ from SMTC models in that the large turbulent eddies are explicitly resolved in the LES down to the grid resolution and only the smaller eddies are modeled or parameterized, so it can better resolve the turbulence in the water column. The NCAR LES model has been shown to accurately reproduce observed upper ocean responses to different meteorological forcing and oceanic conditions (Kukulka et al., 2009; Liang et al., 2013, 2017; Fan et al., 2018, 2020). In the simulation at OSP, the observed temperature and salinity variations in the water column are also well represented by the LES model during the 15-day simulation period (Fig. 1d–f). Since there are no observations of the turbulence structures at OSP, the LES simulated turbulence is used to evaluate the performance of the SMTC models.

MLD (defined as the depth where changes of the potential density referenced to surface are less than 0.1 kg/m^3) estimated by the LES simulation is also used to evaluate the NCOM simulated MLD since the vertical resolution of the temperature and salinity measurements are coarse (see black dots in Fig. 1e and f for measurement depth).

3. Results

3.1. Vertical grid and resolution dependence of the SMTC models

The UG and USG grid options are currently implemented in NCOM. While the UG grid is easier to apply, the USG grid is usually preferred because its finer resolution in the upper layers can better resolve the vertical structure of the flow field generated by the imposed surface forcing. As expected, for both grid types, higher resolution (more

Table 1
Root mean square error of sea surface temperature (SST) relative to observations and mixed layer depth (MLD) relative to LES results for all NCOM experiments include three turbulent mixing schemes (MY2.5, KC04, and H15) with different grid types and resolution. The green and red shaded cells indicate the minimum and maximum errors for SST and MLD for each scheme.

	Layers	30		40		50		80		100	
	Var. / Grid	SST (°C)	MLD (m)	SST (°C)	MLD (m)	SST (°C)	MLD (m)	SST (°C)	MLD (m)	SST (°C)	MLD (m)
MY2.5	UG	0.36	11.27	0.36	10.73	0.35	10.0	0.35	9.78	0.35	9.54
	USG	0.36	11.36	0.36	11.26	0.35	10.66	0.34	9.69	0.34	9.56
	MLEG	0.35	9.57	0.35	9.55	0.35	9.55	0.34	9.09	0.34	9.09
KC04	UG	0.34	9.70	0.35	9.70	0.34	9.26	0.34	8.98	0.34	8.81
	USG	0.35	10.11	0.34	9.77	0.34	9.14	0.34	8.77	0.34	8.63
	MLEG	0.34	8.82	0.34	8.82	0.34	8.81	0.33	8.38	0.33	8.38
H15	UG	0.32	9.01	0.32	8.39	0.32	8.37	0.32	7.70	0.32	7.66
	USG	0.33	9.71	0.33	8.61	0.32	8.42	0.32	7.82	0.32	7.60
	MLEG	0.32	7.68	0.32	7.68	0.32	7.68	0.32	7.27	0.31	7.11

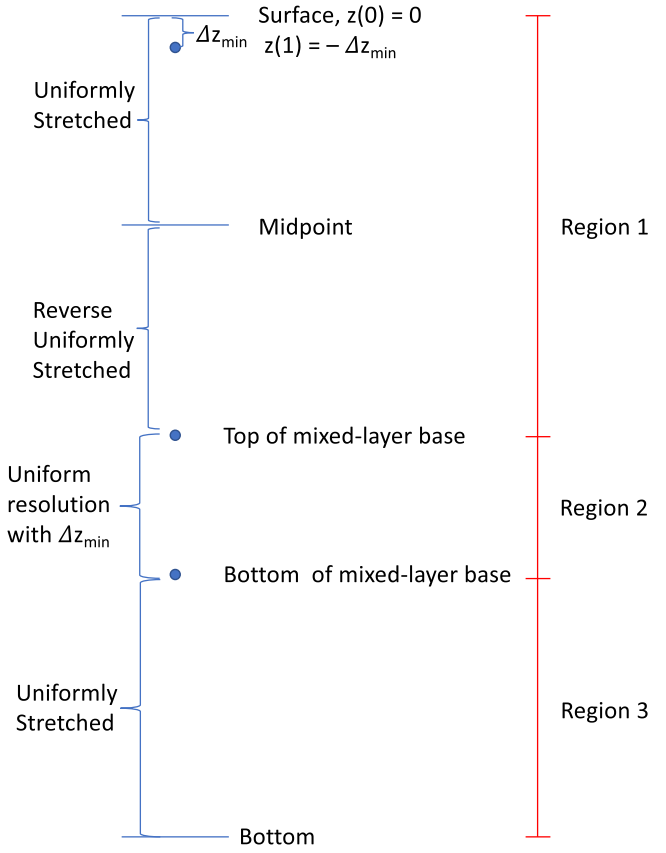

Fig. 3. Design of the mixed layer enhance grid. Δz_{min} is the minimum grid resolution that is used for the first layer at surface and within the base of the mixed layer.

layers) gives smaller MLD error relative to the LES result for all three turbulent closure models (Table 1, Fig. 2b–d), while the differences in SST errors are relatively small among different resolutions.

Table 1. Root mean square error of sea surface temperature (SST) relative to observations and mixed layer depth (MLD) relative to LES results for all NCOM experiments include three turbulent mixing schemes (MY2.5, KC04, and H15) with different grid types and resolution. The green and red shaded cells indicate the minimum and maximum errors for SST and MLD for each scheme.

Interestingly, for low resolution (30 or 40 layers) simulations, larger MLD errors are found in experiments using the USG grid than that using the UG grid, even though the USG grid uses much higher surface resolution (Fig. 2a). Especially towards the end of the simulation, the MLD in the UG30 experiment is ~1 m deeper than that in the USG30 experiment for both the KC04 and H15 schemes (Fig. 2c and 2d). A ~0.5 m deeper MLD in the UG40 experiment than the USG40 experiment was also observed for the MY2.5 and H15 model (Fig. 2b and d). Since the UG30/40 grid provides higher resolution near the base of the mixed layer than the USG30/40 grid (Fig. 2a), it could be the reason for the better model performances.

While finer resolution near the surface is always attempted by ocean modelers, the resolution near the base of the mixed layer is often overlooked. To better understand its effect on mixed layer simulations, a new type of vertical grid, the mixed layer enhanced grid (MLEG), is designed so that the same high resolution (2 m for 30, 40, and 50 layers and 1 m for 80 and 100 layers) is used both at the water surface and near the bottom of the mixed layer from 60 to 80 m depth (Fig. 2a solid lines).

Large improvements in MLD simulations are observed using the MLEG grid (Table 1, Fig. 2). Especially for the experiments with lower number of vertical layers, up to 2–3 m of deepening are found in the MLEG experiments relative to the UG or USG experiments (Fig. 2b–d, solid lines). Large reductions in root mean square errors are recorded in the MLEG30 experiment relative to the UG30/USG30 experiment (1.7 m and 1.79 m error reduction respectively) when the MY2.5 scheme is used (Table 1). Also notice that the model simulated SST and MLD accuracy in the MLEG30 experiments are as good as the UG100 and USG100 experiments for all three SMTC models. This suggests that using higher resolution near the base of the mixed layer can help us archive higher model accuracy with much lower number of vertical layers and thus a much lower computational cost.

It is interesting to find that the simulated MLD in the MLEG30, MLEG40, and MLEG50 experiments are very similar to each other for all three SMTC models (Fig. 2b–d). The MLD in the MLEG80 and MLEG100 experiments are also visually identical for the MY2.5 and KC04 schemes with MLEG100 slightly deeper than MLEG80 when the H15 scheme is used. The root mean square error of MLD and SST also show the same characteristics (Table 1). This feature suggests that resolution at the surface and near the base of the mixed layer is more important than resolution within the middle of the mixed layer. Simulations using the MLEG grids will give very similar accuracy when the same resolution is used at the surface and the base of the mixed layer (from 60 to 80 m

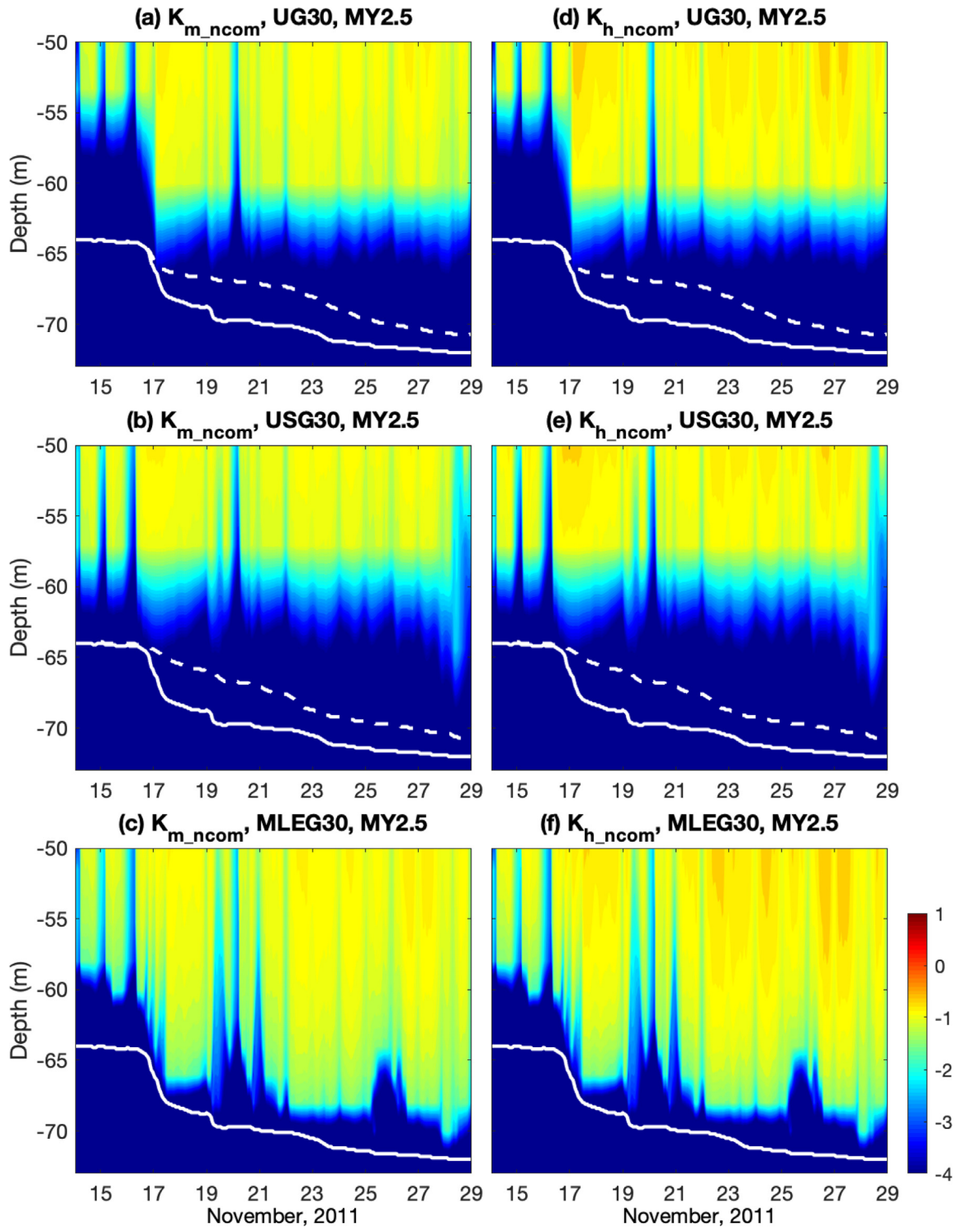

Fig. 4. The log10 of eddy viscosity (K_{m_ncom}) from experiments (a) UG30, (b) USG30, and (c) MLEG30 using the MY2.5 scheme, and the log10 of eddy diffusivity (K_{h_ncom}) for experiments (d) UG30, (e) USG30, (f) MLEG100 using the MY2.5 scheme. The dashed white lines in panels (a), (b), (d) and (e) give the MLD in the experiment presented, and the solid white lines in all panels represent the MLD from the MLEG30 experiment.

depth in our case). The number of layers used within the middle of the mixed layer has very small effect on the MLD accuracy.

To understand the reason for mixed layer deepening using the MLEG grids, we diagnose the eddy viscosity (K_{m_ncom}) and diffusivity (K_{h_ncom}) from the NCOM experiments calculated as

$$K_{m\_ncom} = lqS_M \tag{2}$$

$$K_{h\_ncom} = lqS_H \tag{3}$$

Here q is the square root of twice the TKE ($= \frac{1}{2}q^2$), l is the turbulent length scale, and $S_H = \frac{C_1}{1-C_2G_H}$ and $S_M = \frac{C_3+C_4 S_H G_H}{1-C_2G_H}$ are the stratification functions used to describe the effect of stratification on vertical mixing. Both K_{m_ncom} and K_{h_ncom} are highly dependent on the vertical gradients of current and density in the mixed layer because: (a) l and $\frac{1}{2}q^2$ are solved by the prognostic equations (given in Appendix) derived by Mellor and Yamada (1982), and are sensitive to the resolved

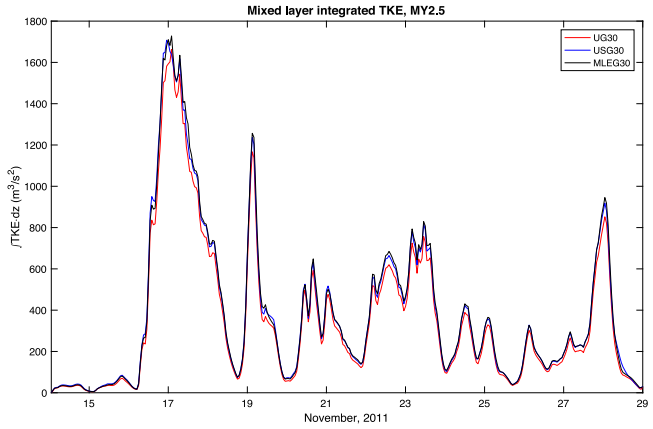

Fig. 5. Mixed layer depth integrated TKE for experiments UG30, USG30, and MLEG30.

vertical shear of currents and density in the mixed layer; (b) Since C_1 to C_5 in S_H and S_M are empirical constants (given in Appendix), S_H and S_M only vary with the stratification $G_H = min\left[0.028, \frac{l^2 g}{q^2 \rho_0} \frac{\partial \bar{\rho}}{\partial z}\right]$ and thus also depend closely on the resolved vertical density ($\bar{\rho}$) shear in the water column. Here, the maximum value of G_H is set to be 0.028 based on Mellor (2001) in which the author found that "The stability functions limit to infinity as G_H approaches the value 0.0288". 0.028 is used in NCOM to keep S_H and S_M within a reasonable range.

We only analyze the 30-layer experiments using the MY2.5 scheme here since they show the largest differences among different grid types. As we can see from Fig. 4, for the same grid, the structure and time variation of K_{h_ncom} and K_{m_ncom} are very similar to each other with small magnitude difference. Thus, we will only focus on the structure of K_{m_ncom} in this section.

In the UG30 and USG30 experiments, the vertical grid resolution around the base of the mixed layer ranges from 7 to 10 m. The coarse vertical resolution results in poor representation of the density structures and underestimation of currents in the region that leads to weaker turbulence, and the eddy viscosity diminishes several meters above the base of the mixed layer (Fig. 4a and b). While in the MLEG30 experiment, with the much finer resolution (2 m) around the base of the mixed layer, the current and density gradients are adequately resolved in the region, which leads to enhanced turbulence, deeper eddy viscosity penetration, and consequently deepening of the mixed layer (Fig. 4c). Especially during the strong cooling event on November 16, a corresponding sharp deepening of ~5 m is observed in experiment MLEG30, while USG30 only shows a mild gradual deepening of ~1–2 m.

As Grant and Belcher (2011) has pointed out, the vertical gradients of the current velocity change rapidly with depth in the stratified shear layer from above the base of the mixed layer to the base of the boundary layer, and thus creates a maximal shear turbulence close to the base of the mixed layer. Being able to better resolve the current structure there leads to a better representation of the shear turbulence in the mixed layer, which is clearly associated with the exchange of heat and momentum between the mixed layer and the thermocline below. Since the variation of K_{m_ncom} and K_{h_ncom} with depth are small in the middle of the mixed layer (see Fig. 6 for example), the vertical resolution in that region has minimal effect on the modeled turbulence in the mixed layer. That is why we see almost identical model solutions from experiment MLEG30, MLEG40, and MLEG50 (Fig. 2).

Note that while the MLEG30 experiment gives slightly higher mixed layer integrated TKE than UG30, its total TKE is almost the same as USG30 (Fig. 5). This is because most of the TKE in the water column is confined in a thin layer near the surface. Since both MLEG30 and USG30 use much finer resolution (2 m and 1 m respectively) at the surface than UG30 ($\Delta z = 6.7$ m), they can better resolve the TKE input. This is one of the reasons for the preference of higher resolution near surface in ocean circulation models.

Notice that not only the experiments using the KC04 and H15 schemes produce deeper mixed layers than that using the MY2.5 scheme, the MLD differences between the experiments using the UG/USG grids and that using the MLEG grids are also smaller for these two SMTC models (Fig. 2, Table 1). This is because, for the KC04 and H15 models, there are two distinct turbulent processes in the boundary layer, the shear turbulence and the Langmuir turbulence. While the solution of the shear turbulence is highly dependent on the vertical resolution near the base of the mixed layer as shown above, the vertical profile of the Stokes drift that determines the magnitude of the Langmuir turbulence is derived from observations and not affected by the vertical resolution in the model. Thus, while the added Langmuir turbulence worked to further deepen the mixed layer in the KC04 and H15 models, the overall effect of vertical resolution on the mixed layer turbulence is relatively smaller in these two turbulent closure models.

3.2. Near inertial gravity waves beneath the mixed layer

Although the MLEG grids can help deepen the mixed layer relative to the UG and USG grids, the resulted MLD is still much shallower than the LES result (Fig. 1g). To better understand the reason for the discrepancy, we compare K_{m_ncom} in experiments MLEG100 using the three SMTC models with the eddy viscosity from the LES simulation, K_{m_les}, which is calculated using the Reynolds stress and mean shear following McWilliams et al. (2012):

$$K_{m\_les} = \frac{\left|\langle \boldsymbol{u}' w \rangle\right|}{\left|\partial_z \langle \boldsymbol{u}^L \rangle\right|} \tag{4}$$

Here, $\langle \boldsymbol{u}' w \rangle$ is the horizontal domain averaged total Reynold stress, and $<\boldsymbol{u}^L>$ is the horizontal domain averaged Lagrangian velocity (mean current plus Stokes drift).

As we can see in Fig. 6, the H15 scheme gives the largest K_{m_ncom} in the mixed layer among the three SMTC models. It can provide similar magnitude of eddy viscosity as the LES model within the mixed layer with even deeper depth penetration of high values (Fig. 6c and d). However, the turbulence in the H15 model is much weaker (lower than 10^{-4}) beneath the mixed layer than that in the LES simulations. Part of the reason for the weaker turbulence in these Mellor–Yamada type models is that they assume parameters governing the degree of anisotropy are small, thus the turbulence beneath the mixed layer is underestimated in stably stratified fluids. Another reason that is mainly responsible for the weak turbulence beneath the mixed layer is that the SMTC models cannot represent the effect of the downward propagating near inertial gravity waves as demonstrated by the LES in its mean flow (averaged over the horizontal domain) fields given in Fig. 7. These waves are recognizable by their characteristic circularly polarized velocities, and their strong shear is a major contributor to upper-ocean mixing and can affect a variety of dynamic processes (Jochum et al., 2012).

The frequency (f) spectrum of the x direction horizontal velocity, $S_{xx}(f)$, at a depth 2 m below the deepest MLD during the simulation period reveals a strong peak at 15.60 h (Fig. 8, blue line), a little shorter than the inertial period of 15.62 h at OSP. The shape of the velocity spectrum in our study is very similar to the observed velocity spectra by D'Asaro (1985) collected close to OSP during the Ocean Storms Experiment in the North Pacific, except the peak energy in our study is much higher due to the stronger wind forcing experience during our study period (maximum wind exceeded 20 m/s in our study vs. less than 10 m/s in their study). Note that our results do not show the two small peaks at the semidiurnal tidal frequency and the frequency band that is twice the inertial frequency as in D'Asaro (1985). The wave energy in the double inertial frequency band is generated by the interaction between mesoscale eddies and the near inertial currents. Filamentary structures that are characterized by negative vorticity anomaly can trap

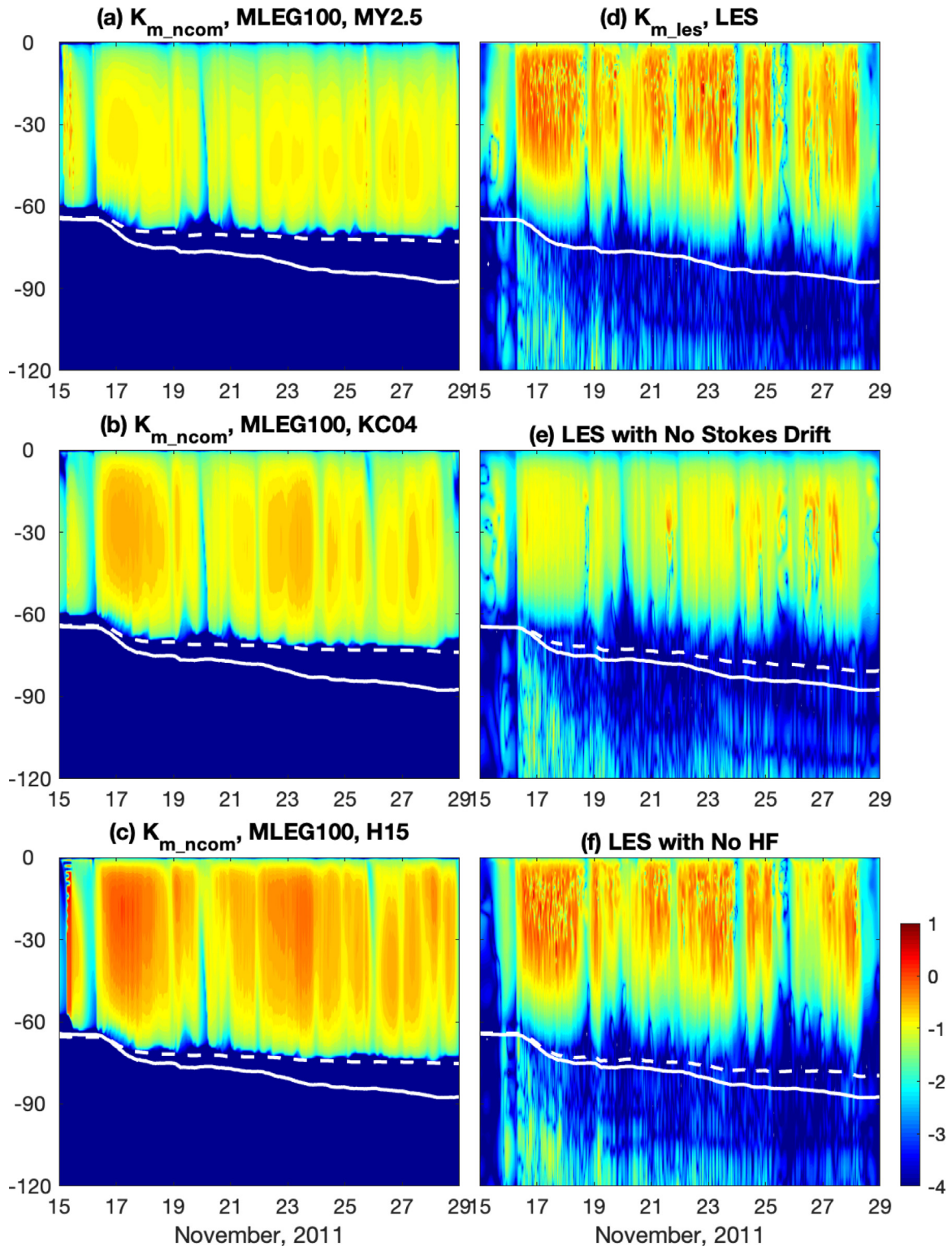

Fig. 6. The log10 of eddy viscosity from experiments MLEG100 using (a) MY2.5, (b) KC04, and (c) H15 schemes, and from LES experiments (d) with all forcing, (e) without Stokes drift, and (f) without heat flux. The dashed white lines in the panels represent MLD from the experiment presented and the solid white lines in all panels represent the MLD in the LES experiment with all forcing.

the near inertial waves and generate waves of multiples of fundamental inertial frequency (Danioux and Klein, 2008; Danioux et al., 2008; Kawaguchi et al., 2020). Since our LES simulations do not include the effect of mesoscale eddies and tides, waves in these two frequency bands are not simulated. However, as suggested by D'Asaro (1985), the wave energies in these two frequency bands are two orders of magnitude lower than that in the near inertial band, and thus has negligible effect on the turbulent mixing in the water column.

To understand the relative fraction of variance within this near inertial band of frequencies relative to other band of frequencies. The Variance-preserving spectra, $S_{xx}(f)$ times frequency f, as a function of $\log(f)$ are given in Fig. 8b following Emery and Thomson (2004). The

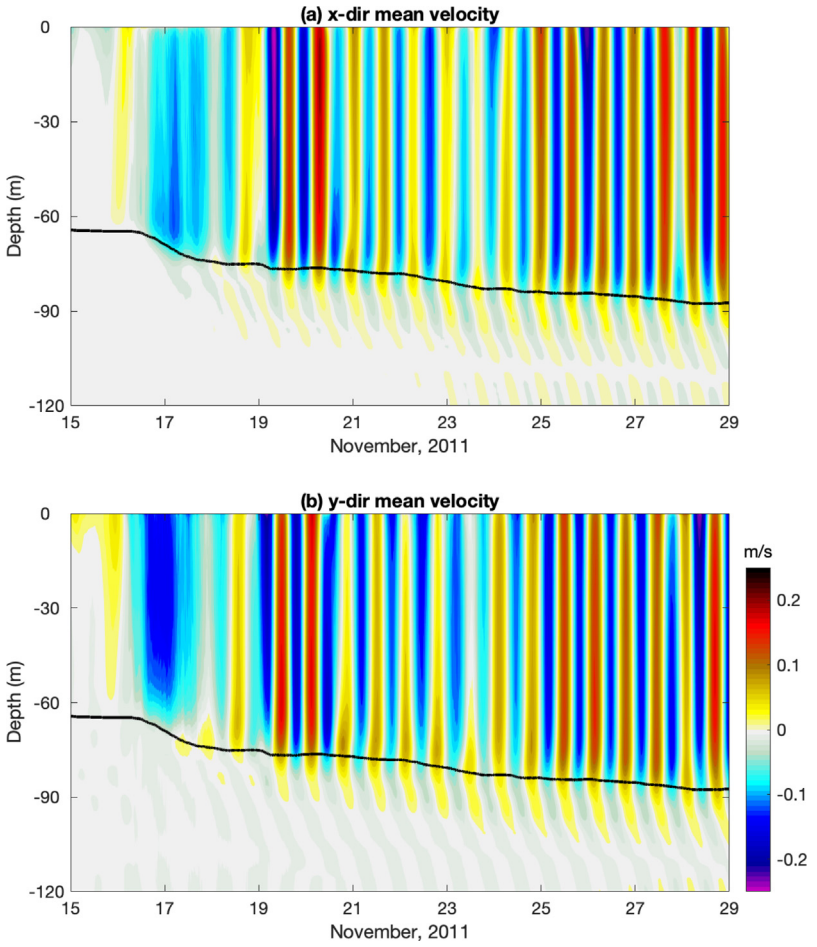

Fig. 7. (a) x and (b) y direction domain mean velocity in the LES experiment with all forcing. The black line represents the MLD in the simulation.

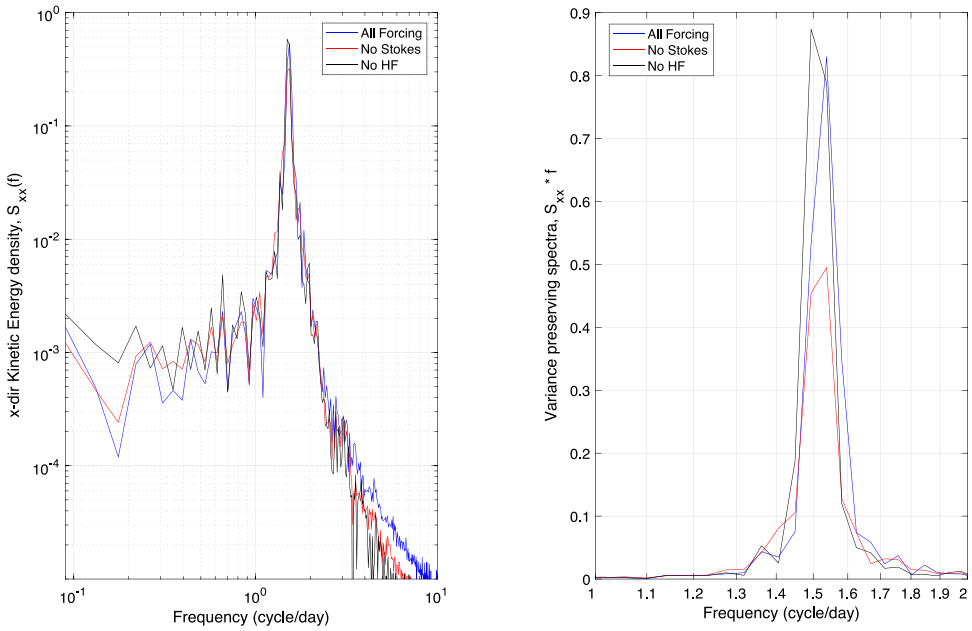

Fig. 8. Kinetic energy spectrum of x direction current, $S_{xx}(f)$ at 2 meters below the maximum MLD (left), and its associated variance preserving power spectra ($S_{xx}(f)$*f) (right).

area under the spectral curve between two frequencies (i.e. f_1 and f_2) thus gives a measure of the spectral signal variance in that frequency band:

$$\sigma^2 = \int_{f_1}^{f_2} f S_{xx}(f)\, d(log(f)) = \int_{f_1}^{f_2} S_{xx}(f)\, df \quad (5)$$

We can see that the near inertial motions are the dominant energy source in the velocity field. These near inertial waves have an upward phase propagation and thus a downward energy propagation. As opposed to pure inertial motions that are horizontal, these slightly super-inertial motions have vertical displacements that can modulate the stratification via the wave strain and thus the water column stability (Alford et al., 2016). Several observational studies (Plueddemann and Farrar, 2006; Johnston and Rudnick, 2009; Dohan and Davis, 2011; Sanford et al., 2011) have found that the near-inertial motions can result in shear across the transition layer that separates the mixed layer from the stratified waters below, and is a major mechanism for mixing and deepening of the mixed layer following storms.

Since the momentum and heat diffusivities below the mixed layer are treated as adjustable parameters for the SMTC models discussed in this study, the effect of near inertial waves is minimized and thus limited their ability to further deepen the mixed layer. Furthermore, these SMTC models neglected the material derivative and diffusion terms in the density equations in order to simplify the model (Mellor and Yamada, 1982), and thus the downgradient approximation in these models seriously underestimates the third-order moments (Canuto et al., 2001). As a result, while the SMTC models can be justified for stable and slightly unstable flows, the scheme is more likely to promote errors in highly unstable conditions, such as the deep convection induced by the strong cooling on November 16.

While some studies (D'Asaro et al., 1995; Alford, 2003) suggested that these near inertial motions are linked to the wind stress impulses associated with midlatitude storms that typically contain strong inertially rotating components, inertial currents advecting Langmuir cells over the stratified interior is another suggested cause for these waves (Polton et al., 2008). To test this theory, a new LES experiment without Stokes drift was conducted. We can see that the near inertial motions beneath the mixed layer are much weaker without the presence of Langmuir turbulence (Fig. 9). While the frequency spectrum still shows a dominant peak at 15.60 h, its peak energy is much lower than the experiment with Stokes drift (Fig. 8a), and the total energy within the near inertial band has been reduced by almost half (Fig. 8b). This suggests that both the wind shear and the interaction between Langmuir cells and the inertial currents are important for the strength of the near inertial waves. While they can be generated by the wind stress impulses alone, the presence of surface gravity waves can significantly enhance the magnitude of the waves. Also notice that the mean currents in the mixed layer become stronger without Stokes drift, especially near the surface. This is because the circular motion of the Langmuir cells and the added anti-Stokes transport by the Stokes–Coriolis force in the along wind direction work together to reduce the downwind velocity near the surface, and as a result, the mean currents become more uniformly distributed with depth (McWilliams et al., 1997, 2012). It is interesting to notice that while the eddy viscosity in the mixed layer is greatly reduced in the experiment without Stokes drift, the magnitude of the eddy viscosity beneath the mixed layer does not show significant changes (Fig. 6e).

As discussed earlier, there are several cooling events during our simulations period. Especially on November 16, a large net cooling flux of ~450 W m^{-2} was observed primarily due to the strong sensible and latent heat fluxes at the ocean surface (Fig. 1c). Since we are not aware of any research that investigates the possible effect of surface heat fluxes on the near inertial gravity waves beneath the mixed layer, we will take this opportunity to study its impact here. For this purpose, one more LES experiment is conducted that uses only the wind and Stokes forcing with the net heat flux set to zero during the entire simulation period. We can see that while the mean currents in the mixed layer have very similar structure and magnitude as the experiment with the heat flux, the removal of the net heat flux in the simulation has led to stronger near inertial motions beneath the mixed layer (Fig. 10). There are two possible reasons for this enhancement. Firstly, since the mixed layer depth is shallower in the experiment without heat flux, the Stokes drift velocity that decays with depth is larger at the base of the mixed layer. Secondly, as Fan et al. (2020) have suggested, the upwelling associated with Langmuir circulation at the base of the mixed layer and the downwelling associated with the deep convection triggered by the surface cooling may counteract on each other, and hence, the removed of the surface cooling has further enabled stronger Langmuir circulation at the base of the mixed layer. Notice that the peak of the horizontal velocity frequency spectrum is shifted slightly towards lower frequency of 16 h instead of 15.60 h when the net heat flux is removed from the forcing (Fig. 8a), and the near inertial band is slightly wider than that in the experiment with all forcing and thus contains more kinetic energy in the wave train (Fig. 8b). While the magnitude of the eddy viscosity remains similar to the experiment with all forcing, its penetration depth within the mixed layer is shallower when the surface heat flux is removed from the simulation (Fig. 6f). This is due to the absence of deep convection associated with surface cooling that has led to reduced mixing and thus shallower mixed layer. However, like the experiment without Stokes drift, the magnitude of the eddy viscosity beneath the mixed layer does not show significant changes either when net heat flux is removed from the simulation (Fig. 6f). This feature suggests that there is a possibility to parameterize the effect near inertial gravity waves in the eddy viscosity beneath the mixed layer without having to involve complicated dynamics such as the Langmuir turbulence or deep convection.

4. Discussion and conclusions

This study investigated the coordinate and resolution dependence of the Mellor and Yamada (1982) level 2.5, the Kantha and Clayson (2004), and the Harcourt (2015) turbulent closure models through one-dimension NCOM experiments and large eddy simulation studies using observed meteorological forcing and oceanic conditions at Ocean Station Papa (OSP). Model results suggest that finer resolution near the base of the mixed is critical for the representation of turbulence in the turbulent closure models because it can better resolve the current gradients near the mixed layer base. A mixed layer enhanced vertical grid (MLEG) is proposed which uses the same high resolution both at the water surface and near the bottom of the mixed layer (from 60 to 80 m depth for the OSP case). NCOM experiments using the new grid outperform both the uniform and stretched grids even with significantly fewer vertical layers used. It is found that when using the MLEG grid, the model accuracy is strongly dependent on the resolution near the base of the mixed layer while the total number of vertical layers used in the mixed layer has minimum effect.

Given the improvements in MLD simulations using the MLEG grids, the second moment turbulent closure models still have hard time deepening the mixed layer relative to large eddy simulations. Although the assumption of small/negligible anisotropy in these models can be partially blamed for the weaker turbulence, the most likely major reason is the lack of representation for the near inertial gravity waves below the mixed layer. These slightly super-inertial motions have vertical displacements that can modulate the stratification via the wave strain and thus the water column stability, which is very important for mixing. While both the Langmuir circulation and the variation of surface heat fluxes can impact the strength of these waves, the magnitude of the eddy viscosity beneath the mixed layer does not show significant changes with either dynamical processes.

Another weakness of the SMTC models evaluated in this study is their small critical Richardson number (Ricr) that usually lead to shallower boundary layer predictions (Cheng et al., 2002). As pointed

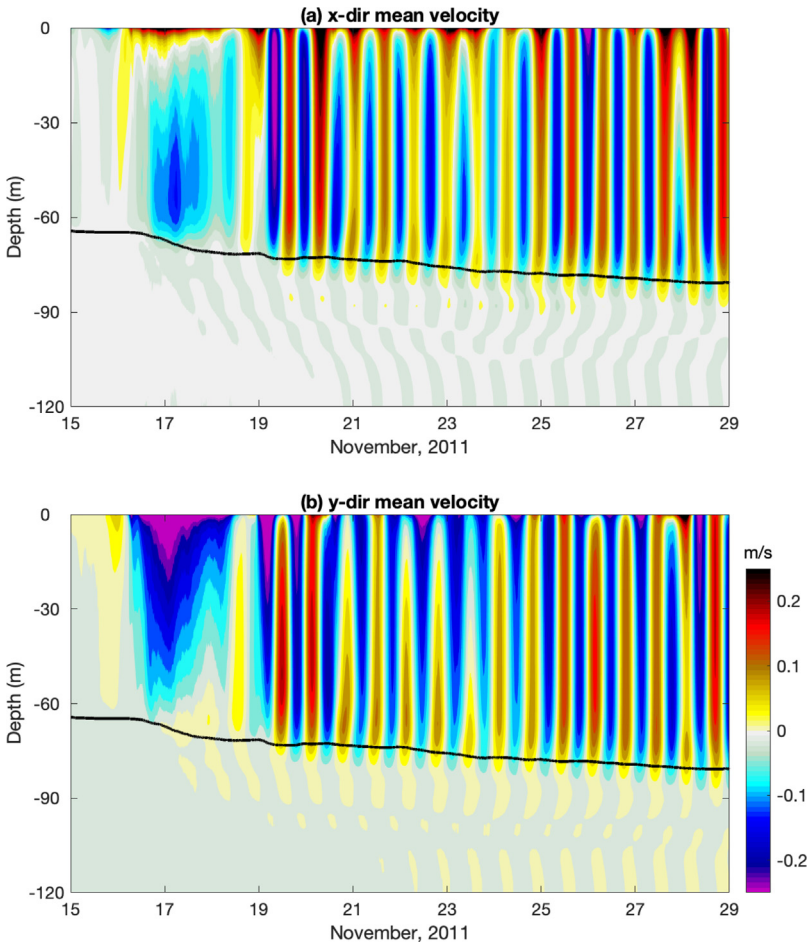

Fig. 9. (a) x and (b) y direction domain mean velocity in the LES experiment without Stokes drift. The black line represents the MLD in the simulation.

out by Canuto et al. (2008), turbulent mixing exists up to Richardson number Ri ~ O(100), hence there is practically no Ricr. New turbulent closure models were thus proposed to extend the Ricr to infinity for planetary boundary layer models, such as Zilitinkevich and Esau (2007), Canuto et al. (2008), and Kantha and Carniel (2009). But these models were more complicated than the MY2.5 model and not as efficient as the Galperin et al. (1988) model.

Recently, Cheng et al. (2020) formulated a new turbulent closure model for the planetary boundary layer that extends the Ricr to infinity through the derivation of a new set of heat flux equations that parameterize the length scale ratio as a function of second moments instead of a constant. Although the new model is developed based on the MY2.5 and Galperin et al. (1988) models, it is structurally simpler, and its results are compared favorably with meteorological, experimental, DNS and LES data. A generalized model from Cheng et al. (2020) that includes salinity will be a promising development for turbulence mixing schemes in the ocean circulation models.

CRediT authorship contribution statement

Yalin Fan: Conceptualization, Methodology, LES simulation, Visualization, Investigation, Writing – original draft. **Zhitao Yu:** NCOM evaluation, Visualization, Investigation, Writing – review & editing. **Gregg Jacobs:** Investigation, Writing – review & editing.

Declaration of competing interest

The authors declare that they have no known competing financial interests or personal relationships that could have appeared to influence the work reported in this paper.

Acknowledgments

We would like to express our appreciation to the anonymous reviewers for their constructive comments. Computations for this study were performed at the Navy DoD Supercomputing Resource Center (DSRC). Y. Fan was funded by the Office of Naval Research under program element 062435N. Financial support for Z. Yu is provided by the "6.1 South China Sea Dynamics" project sponsored by the Office of Naval Research under program element 0601153N. This paper is a contribution of NRL/JA/7320-20-5038, and has been approved for public release. Data for the analysis and figures in this study were archived at (https://doi.org/10.5281/zenodo.4041938)

Appendix

A.1. Prognostic equations of TKE and length scale

The Mellor and Yamada (1982) 2.5 turbulent closure model uses prognostic equations of energy to solve for the TKE, $\frac{q^2}{2}$, and turbulent length scale l:

$$\frac{D}{Dt}\left(\frac{q^2}{2}\right) - \frac{\partial}{\partial z}\left[lqS_q\frac{\partial}{\partial z}\left(\frac{q^2}{2}\right)\right] = P_s + P_b - \varepsilon \tag{A.1}$$

in which, $P_s = -\langle wu\rangle\frac{\partial U}{\partial z} - \langle wv\rangle\frac{\partial V}{\partial z}$ is the shear production of turbulent energy

$P_b = -\beta g_i\langle u_i\tilde{\rho}\rangle$ is the buoyancy production

$\varepsilon = \frac{q^3}{B_1 l}$ is the dissipation

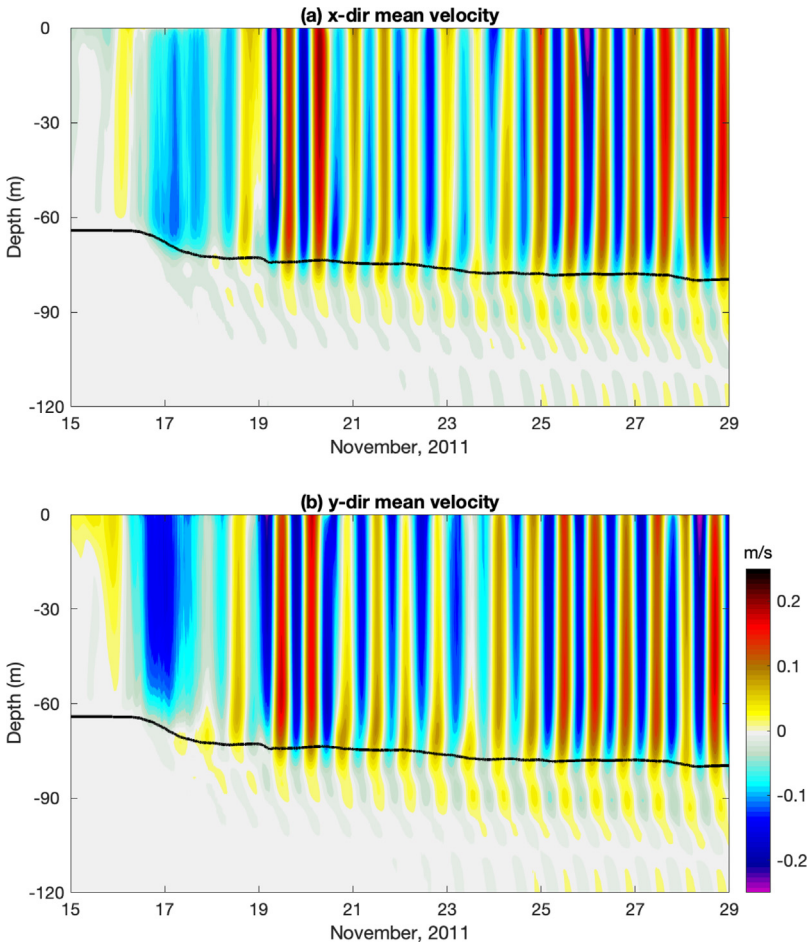

Fig. 10. (a) x and (b) y direction domain mean velocity in the LES experiment without heat flux. The black line represents the MLD in the simulation.

$$\frac{D}{Dt}\left(q^2 l\right) - \frac{\partial}{\partial z}\left[qlS_l \frac{\partial}{\partial z}\left(q^2 l\right)\right] = lE_1\left[P_s + P_b\right] - \frac{q^3}{B_1}\left\{1 + E_2\left(\frac{l}{kL}\right)^2\right\}$$

$$\text{with } L^{-1} = \left(\zeta - z + z_s\right)^{-1} + \left(z - H + z_o\right)^{-1} \tag{A.2}$$

In the above equations, U and V are the mean current velocity in the x and y directions, u_i (u, v, w) are the turbulent current velocity in the x, y, and z directions, $\tilde{\rho}$ is turbulent density fluctuation, ζ is surface elevation, z_s is surface roughness length, z_o is bottom roughness length, and $B_1 = 16.6$, $S_l = 0.2$, $S_q = 0.2$, $E_1 = 1.8$, $E_2 = 1.33$ are constants empirically determined from data. Angle brackets represent ensemble means of turbulent variables.

A.2. Definition of constants in the stratification functions

The stratification functions S_M and S_H used in Eqs. (2) and (3) to describe the effect of stratification on the vertical mixing are given as:

$$S_M = \frac{C_3 + C_4 S_H G_H}{1 - C_5 G_H} \tag{A.3}$$

$$S_H = \frac{C_1}{1 - C_2 G_H} \tag{A.4}$$

Here, the constants C_1 to C_5 are calculated from the basic turbulence constants ($a_1 = 0.92$, $a_2 = 0.74$, $b_1 = 16.6$, $b_2 = 10.1$, and $c_1 = 0.08$) as:

$$C_1 = a_2\left(b_1 - 6a_1\right)/b_1 \tag{A.5}$$

$$C_2 = a_2\left(18a_1 + 3b_2\right) \tag{A.6}$$

$$C_3 = a_1\left(b_1\left(1 - 3c_1\right) - 6a_1\right)/b_1 \tag{A.7}$$

$$C_4 = a_1\left(18a_1 + 9a_2\right) \tag{A.8}$$

$$C_5 = 9a_1 a_2 \tag{A.9}$$

After the substitution C_1 to C_5 given in Eqs. (A.5) to (A.9), Eqs. (A.3) and (A.4) are identical to Eqs. (38) and (39) in Mellor and Yamada (1982) with $\frac{P_s + P_b}{\varepsilon}$ set to equal 1 following Galperin et al. (1988) and Mellor (2001).

Note that the equation for S_M in the NCOM manual (Martin, 2000) has a typo. It should be $C_4 S_H G_H$ on the right hand side of the equation as given in (A.3) instead of $C_4 S_H$ in the NCOM manual.

References

Alford, M.H., 2003. Energy available for ocean mixing redistributed through long-range propagation of internal waves. Nature 423, 159–163.

Alford, M.H., MacKinnon, J.A., Simmons, H.L., Nash, J.D., 2016. Near-inertial internal gravity waves in the ocean. Annu. Rev. Mar. Sci. 8 (2016), 95–123. http://dx.doi.org/10.1146/annurev-marine-010814-015746.

Canuto, V.M., Cheng, Y., Howard, A.M., Essau, E.N., 2008. Stably stratified flows: A model with no Ri(cr). J. Atmos. Sci. 65, 2437–2447. http://dx.doi.org/10.1175/2007JAS2470.1.

Canuto, V.M., Howard, A., Cheng, Y., Dubovikov, M.S., 2001. Ocean turbulence. Part I: one-point closure model. Momentum and heat vertical diffusivities. J. Phys. Oceanogr. 31, 1413–1426.

Cheng, Y., Canuto, V.M., Howard, A.M., 2002. An improved model for the turbulent PBL. J. Atmos. Sci. 59, 1550–1565.

Cheng, Y., Canuto, V.M., Howard, A.M., Acherman, A.S., Kelley, M., Fridlind, A.M., Schmidt, G.A., Yao, M.S., Genio, A.D., Elsaesser, G.S., 2020. A second-order closure turbulence model: New heat flux equations and no critical richardson number. J. Atmos. Sci. 77, 2744–2759.

Craik, A.D.D., Leibovich, S., 1976. A rational model for Langmuir circulations. J. Fluid Mech. 73, 401–426. http://dx.doi.org/10.1017/S0022112076001420.

Danioux, E., Klein, P., 2008. A resonance mechanism leading to wind-forced motions with a 2f frequency. J. Phys. Oceanogr. 38, 2322–2329. http://dx.doi.org/10.1175/2008JPO3822.1.

Danioux, E., Klein, P., Rivi.re, P., 2008. Propagation of wind energy into the deep ocean through a fully turbulent mesoscale eddy field. J. Phys. Oceanogr. 38, 2224–2281. http://dx.doi.org/10.11175/2008JPO3821.1.

D'Asaro, E.A., 1985. The energy flux from the wind to near-inertial motions in the mixed layer. J. Phys. Oceanogr. 15, 1043–1059.

D'Asaro, E.A., Eriksen, C.C., Levine, M.D., Niiler, P., Paulson, C.A., Meurs, P.V., 1995. Upper-ocean inertial currents forced by a strong storm. part I: data and comparisons with linear theory. J. Phys. Oceanogr. 25, 2909–2936.

Dohan, K., Davis, R.E., 2011. Mixing in the transition layer during two storm events. J. Phys. Oceanogr. 41, 42–46.

Emery, W.J., Thomson, R.E., 2004. Data Analysis Methods in Physical Oceanography. Elsevier, p. 638.

Fan, Y., Jarosz, E., Yu, Z., Rogers, E.W., Jensen, T.G., Liang, J.-H., 2018. Langmuir turbulence in horizontal salinity gradient. Ocean Model. 129, 93–103. http://dx.doi.org/10.1016/j.ocemod.2018.07.010.

Fan, Y., Yu, Z., Savelyev, I., Sullivan, P.P., Liang, J.-H., Haack, T., Terrill, E., de Paolo, T., Shearman, K., 2020. The effect of Langmuir turbulence under complex real oceanic and meteorological forcing. Ocean Model. 149, 101601. http://dx.doi.org/10.1016/j.ocemod.2020.101601.

Galperin, B., Kantha, L.H., Hassid, S., Rosati, A., 1988. A quas- equilibrium turbulent energy model for geophysical flows. J. Atmos. Sci. 45, 55–62.

Grant, A.L., Belcher, S.E., 2011. Wind-driven mixing below the oceanic mixed layer. J. Phys. Oceanogr. 41, 1556–1575.

Griffies, S.M., Boning, C., Bryan, F.O., Chassignet, E.P., Gerdes, R., Hasumi, H., Hirst, A., Treguier, A.-M., Webb, D., 2000. Developments in ocean climate modelling. Ocean Model. 2, 123–192.

Harcourt, R.R., 2015. A second-moment closure model of Langmuir turbulence. J. Phys. Oceanogr. 43, 673–697.

Jochum, M., Briegleb, B.P., Danabasoglu, G., Large, W.G., Jayne, S.R., et al., 2012. On the impact of oceanic near-inertial waves on climate. J. Clim. 26, 2833–2844.

Johnston, T.M.S., Rudnick, D.L., 2009. Observations of the transition layer. J. Phys. Oceanogr. 39, 780–797.

Kantha, L.H., Carniel, S., 2009. A note on modeling mixing in stably stratified flows. J. Atmos. Sci. 66, 2501–2505. http://dx.doi.org/10.1175/2009JAS3041.1.

Kantha, L.H., Clayson, C.A., 2004. On the effect of surface gravity waves on mixing in the oceanic mixed layer. Ocean Modell. 6, 101–124.

Kantha, L.H., Lass, U., Prandke, H., 2010. A note on Stokes production of turbulence kinetic energy in the oceanic mixed layer: Observations in the Baltic Sea. Ocean Dyn. 60, 171–180. http://dx.doi.org/10.1007/s10236-009-0257-7, Corrigendum, 60, 629, http://dx.doi.org/10.1007/s10236-010-0283-5.

Kawaguchi, Y., Wagawa, T., Igeta, Y., 2020. Near-inertial internal waves and multiple-inertial oscillations trapped by negative vorticity anomaly in the central Sea of Japan. Prog. Oceanogr. 181, 102240. http://dx.doi.org/10.1016/J.POCEAN.2019.102240.

Kenyon, K.E., 1969. Stokes drift for random gravity waves. J. Geophys. Res. 74 (28), 6991–6994.

Kukulka, T., Plueddemann, A.J., Trowbridge, J.H., Sullivan, P.P., 2009. Significance of Langmuir circulation in upper ocean mixing: Comparison of observations and simulations. Geophys. Res. Lett. 36, L10603. http://dx.doi.org/10.1029/2009GL037620.

Liang, J.-H., Deutsch, C., McWilliams, J.C., Baschek, B., Sullivan, P.P., Chiba, D., 2013. Parameterizing bubble-mediated air-sea gas exchange and its effect on ocean ventilation. Glob. Biogeochem. Cycles 27, 894–905. http://dx.doi.org/10.1002/gbc.20080.

Liang, J.-H., Emerson, S.R., D'Asaro, E.A., McNeil, C.L., Harcourt, R.R., Sullivan, P.P., Yang, B., Cronin, M.F., 2017. On the role of sea-state in bubble-mediated air-sea gas flux during a winter storm. J. Geophys. Res. 122, 2671–2685.

Martin, P.J., 2000. Description of the Navy Coastal Ocean Model Version 1.0. NRL Report No. NRL/FR/7322/00/9962, p. 45, [Available from NRL, Code 7322, Bldg. 1009, Stennis Space Center, MS 39529–5004, USA].

McWilliams, J.C., Huckle, E., Liang, J.-H., 2012. The wavy ekman layer: Langmuir circulations, breaking waves, and reynolds stress. J. Phys. Oceanogr. 42, 1793–1816.

McWilliams, J.C., Sullivan, P.P., Hoeng, C., 1997. Langmuir turbulence in the Ocean. J. Fluid Mech. 334, 1–30.

Mellor, G.L., 2001. One-dimensional, ocean surface modeling, a problem and a solution. J. Phys. Oceanogr. 31, 790–809.

Mellor, G.L., Yamada, T., 1982. Development of a turbulent closure model for geophysical fluid problmes. Rev. Geophys. Space Phys. 20 (4), 851–875.

Metzger, E.J., Helber, R.W., Hogan, P.J., Posey, P.G., Thoppil, P.G., Townsend, T.L., Wallcraft, A.J., Smedstad, O.M., Franklin, D.S., 2017. Global Ocean Forecast System 3.1 Validation Testing. NRL Report NRL/MR/7320–17–9722, p. 59, [Available from NRL, Code 7322, Bldg. 1009, Stennis Space Center, MS 39529–5004, USA].

Plueddemann, A.J., Farrar, J.T., 2006. Observations and models of the energy flux from the wind to mixed-layer inertial currents. Deep-Sea Res. II 53, 5–30.

Polton, J.A., Smith, J.A., MacKinnon, J.A., Tejada-Martinez, A.E., 2008. Rapid generation of high-frequency internal waves beneath a wind and wave forced oceanic surface mixed layer. Geophys. Res. Lett. 35, L13602. http://dx.doi.org/10.1029/2008GL033856.

Rowley, C., Mask, A., 2014. Regional and coastal prediction with the relocatable ocean nowcast/forecast system. Oceanography 27, 3. http://dx.doi.org/10.5670/oceanog.2014.67.

Sanford, T.B., Price, J.F., Girton, J.B., 2011. Upper-ocean response to Hurricane Frances (2004) observed by profiling EM-APEX floats. J. Phys. Oceanogr. 41, 1041–1056.

Send, U., et al., 2010. OceanSITES. In: Hall, J., et al. (Eds.), Proceedings of the OceanObs'09: Sustained Ocean Observations and Information for Society Conference, Vol. 2, Venice, Italy, September 2009. ESA Publ., http://dx.doi.org/10.5270/OceanObs09.cwp.79, WPP-306.

Sullivan, P.P., McWilliams, J.C., Melville, W.K., 2007. Surface gravity wave effects in the oceanic boundary layer: large-eddy simulation with vortex force and stochastic breakers. J. Fluid Mech. 593, 405–452. http://dx.doi.org/10.1017/S002211200700897X.

Thomson, J., D'Asaro, E.A., Cronin, M.F., Rogers, W.E., Harcourt, R.R., Shcherbina, A., 2013. Waves and the equilibrium range at ocean weather station p. J. Geophys. Res. Oceans 118, 5951–5962. http://dx.doi.org/10.1002/2013JC008837.

Zilitinkevich, S., Esau, I.N., 2007. Similarity theory and calculation of turbulent fluxes at the surface for the stably stratified atmospheric boundary layers. Bound.-Lay. Meteorol. 125, 193–206.